SSRG International Journal of Civil Engineering
ISSN: 2348-8352/ https://doi.org/10.14445/23488352/IJCE-V12I12P111

Volume 12 Issue 12, 110-129, December 2025

Original Article

Post-Fire Residual Strength of Cold-Formed Steel Columns Subjected to Realistic Temperature Distribution

Rakshith B. D[1], Punitha kumar A[2]

[1,2]*Department of Structural and Geotechnical Engineering, School of Civil Engineering, Vellore Institute of Technology, Vellore, Tamil Nadu, India.*

[2]*Corresponding Author : punithakumar.a@vit.ac.in*

Received: 08 October 2025 Revised: 12 November 2025 Accepted: 10 December 2025 Published: 29 December 2025

Abstract *- The present study assesses the residual capacity of a steel column after a fire. Altogether 101 numbers of experiments done by earlier studies were taken to validate the numerical model using Abaqus®. The main novelty of the present study includes the evaluation of practical temperature distribution along the length, taken from full-scale fire tests, and superimposing it on validated models to evaluate column capacities. Following validation, extensive parametric studies were conducted to evaluate the column capacity under axial load and uniaxial moment. Comparative analysis found that axially loaded columns subjected to realistic (parabolic) temperature distribution can sustain 40% more load than columns with uniform (idealized) temperature. This increase is 30% for columns with axial load and uniaxial moment. Post-fire column capacities were compared with the standard interaction equation from the European code by merely replacing the post-fire yield strength with the room temperature one. A comparative study of the European code and a parametric study reveal disproportional conservation. In the end, the modified European code model provides an accurate estimation with mild conservation, which can be used by the structural engineering community to assess the realistically heated column capacity.*

Keywords *- Cold-formed steel column, Post-fire strength, realistic temperature distribution, Capacity prediction, Code comparison*.

1. Introduction and Literature Study

Steel columns, unlike reinforced concrete columns, lose strength at a greater pace, leading to early failures. Building fires have increased in recent times due to economic growth, lavish lifestyles, and population concentration in a specific region. Parallel to this, electric automobile usage has increased recently due to low cost and maintenance, and hikes in fuel costs. The usage of electric automobiles (irrespective of two or four wheels) increases the chance of building fires [1]. Buildings such as multi-story car parks and residential buildings with basement parking are affected by these fires. In parking areas, sequentially parked vehicles raise concerns of traveling fires leading to mass ignition (flashover). A chance of ignition is further amplified due to clustered parking spaces in order to increase building occupancy in densely populated cities. In addition to parking fires, unattended electrical switches, and long-term usage of appliances, they also cause fires due to short circuits. The increase in plastic and synthetic products in furniture and room décor amplifies the chances of fire and quick flashovers (a state in which all fuel available in a room ignites instantly). Progressive fires, or fully developed fires, can be suppressed by using automatic fire sprinklers or by firefighters. Once the fire is extinguished, the next step is to assess the damage and level of refurbishment required for the building to safely continue occupancy. Such a scenario demands a residual strength assessment of structural elements with reliability.

In building fires, hot fumes rise up to the ceiling (due to buoyancy), and their place is taken up by cold gas [2]. This process is cyclic, and due to this effect, gas temperature within the building varies along the height. This induces a non-uniform temperature distribution in vertical structures, such as columns, walls, and partitions. In addition, steel-concrete composite floor slabs act as heat dissipaters due to the high specific heat of concrete. This non-uniform temperature along the height is irrespective of column location in the building; hence, it is safe to say that almost all the columns in the building will undergo non-uniform temperature distribution in case of fire accidents. Full-scale fire tests done in the Cardington test facility [2] validate the non-uniform distribution. Figures (1, 2). Among six full-scale tests conducted on an eight-story steel composite framed building at Cardington, the corner compartment test (or Test-3) is selected for the present study. The test consists of 4 columns and wooden cribs for fire loading. To idealize the

temperature distribution by all 4 columns, the ratio of temperature (t_i/t_{max}) and column height was normalized (max. = 1) (Figure 2). Interested readers can look into experiments done on a full-scale fire test done at Cardington [2]. In addition to the Cardington fire tests, a full-scale open fire test conducted on a steel portal frame by Ji et al. [3] shows a non-uniform distribution, as shown in Figure 2.

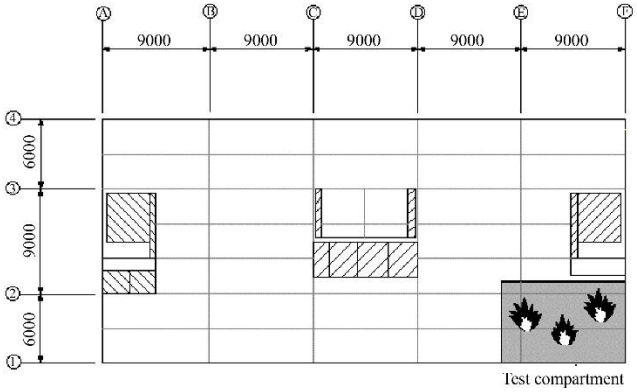

Fig. 1 Layout of Cardington fire test (corner compartment [2]

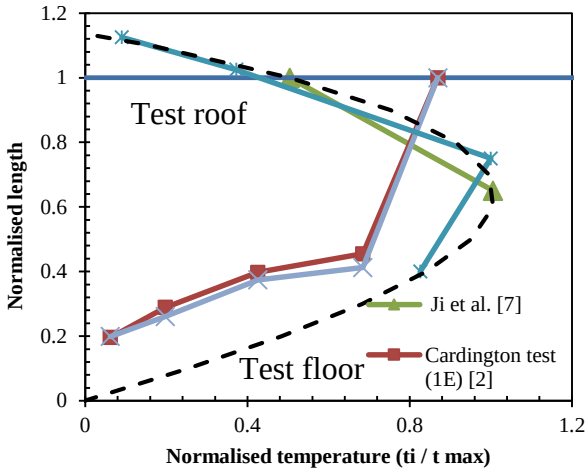

Fig. 2 Realistic temperature distribution [2, 7]

Steel consumption in India has increased over the decade; this is due to its quick erection and competitive pricing in the local market. A large portion of transportation terminals, such as railways, airports, and bus shelters in India, adopt steel. In addition to commercial buildings, residential buildings ranging from low to mid-rise apartments use cold-formed steel for ease of fabrication and quick erection. One such example is shown in Figures 3 and 4, showcasing cold-formed steel used as both beams and columns. Presently, no code [3-5] gives either guidelines or a design procedure to determine the residual strength of fire-surviving structures. In addition, reusing steel structures after fire leads to sustainability, which is goal 11 among 17 sustainable development goals as per [6]. Hence, to address all these fundamental needs, the present study deals with the residual strength assessment of cold-formed steel columns after fire.

Earlier studies consisting of experimental post-fire column strength and material properties are briefly dealt with here. The first experiments on post-fire column capacity were done by Wang and Liu [8]. The author's test consisted of 4 high-strength (Q-460) welded box and I-shaped columns after ISO-834 [9] fire. Test results showed that there was a considerable reduction in column strength after subjecting it to high temperature (900°C). Han et al. [10] tested 51 stub square hollow columns after fire. Their study showed that heating duration has no effect on column capacities. Ma et al. [11] tested 32 post-fire mild steel circular columns under compression after ISO-834 [9] fire. Test results showed no major reduction in column strength up to 700°C, after which a 78% reduction is observed at 1000°C. He et al. [12] tested 16 circular hollow stainless steel stub columns after fire. Test results show no reduction in strength until 600-800°C, after which a steep reduction till 1000°C was reported. He et al. [13] tested 60 square stainless steel stub columns after fire. The test consisted of slender cross-sections with varying thickness. Among water- and air-cooled specimens, water-cooled specimens showed a higher reduction in strength. He et al. [14] tested 15 circular stainless steel stub columns after fire. Test results show a minor change up to 600°C, and after that, a reduction of 30% in column capacity was observed at 1000°C. Li et al. [15] tested 3 high-strength (Q-550) I-shaped restrained columns after fire. Test results showed that the column buckled at temperatures as low as 300°C when restrained, and residual deformation had a major influence on post-fire column capacities compared to material degradation. The study also found that steel grade had no influence over post-fire restrained column capacity. Zong et al. [16] tested 10 high-strength (S-700) square stub columns under eccentric loading after fire.

Tests showed mild variation of column capacity till 600°C, but after that, a 60% steep loss in strength is observed at 1000°C. Zong et al. [17] tested 15 high-strength (S-700) square and rectangular stub columns under compression in order to explore cross-sectional behavior. The cross-sectional slenderness limit provided by the European code [3], the American specification [4], and the Australian standard [5] proved to be fair, with the Australian standard [5] showcasing the highest accuracy. Su et al. [18] tested 21 high-strength (S-690) welded I-shaped stub columns under compression after fire. Similar to earlier studies on cold-formed closed sections, the author's present study also showed a minor change in column capacity at 600°C, but with 52% of capacity reduction at 950°C. Su et al. [19] tested 14 ultra-high-strength (S-960) welded I-shaped stub columns under compression after fire. Tests aiming to compare local plate buckling capacity after fire with standards like the European code [3], the American specification [4], and the Australian standard [5] proved to be accurate till 700°C, but after that, code capacities were too conservative till 1000°C. Zong et al. [20-23] tested 35 high-strength (S-700) cold-formed circular intermediate columns under axial and eccentric compression.

The grouped study consisted of stub and intermediate columns, and the loss of strength for concentrically and eccentrically loaded columns was within the range of 58-64%. A parametric study was done using test results, which were compared with standards and codes. Zuo et al. [24] tested 18 cold-formed elliptical oval sections under compression after subjecting them to the ISO-834 [9] fire curve. The test series consisted of 3 types of cross-sections and 4 levels of temperature exposures. In contrast to earlier studies at 550°C, a considerable reduction in strength is observed, and at 900°C, the column lost 37% of its strength. Zuo et al. [25] tested 17 cold-formed semi-oval stub columns after ISO-834 [9] fire. Unlike the fully oval section reported by previous literature, semi-oval stub column reduction was limited to 30% after 900°C.

Wang et al. [26] tested 8 ultra-high-strength (Q-960) steel columns under compression after fire. Global slenderness ratios of short to slender were selected to test specimens. A study showed that the loss of short column strength (26%) was twice as much as that of slender columns (13%) at 900°C. Zhang et al. [27] tested 18 ultra-high-strength (S-890) steel stub columns under eccentric loading conditions after fire. Similar to normal-strength steel studies done earlier, ultra-high-strength steel also had a minor variation of capacity till 600°C, but at 1000°C, a loss of 51% is obtained. Codes and standards [3-5] whose applicability is limited to high-strength steel (700 MPa) were used to determine the capacity of ultra-high-strength steel, which provided a conservative comparison. Zhang et al. [27] tested 18 nos. of post-fire ultra-high strength (S-890) steel intermediate columns under eccentric loading. Although the grade of steel was similar to previous literature, the loss of strength obtained is 63.48%, which is more than that of stub columns at 1000°C.

Fig. 3 C.F.S. square sections used as beams and columns

All column tests done by earlier studies [7-27] were preceded by post-fire tension tests. Both column strength and yield strength varied slightly till 600°C, following which a steep reduction is observed till 1000°C. All studies presented previously adopted a uniform temperature distribution along column height, which is ideal but not practical. The present study deals with the axial load-carrying capacity of columns under realistic temperature distribution obtained by utilizing the temperature field obtained by previous full-scale tests. The study discusses the effect of temperature idealization and draws capacity estimation for steel columns under realistic temperatures.

Fig. 4 Overview of (G+2) commercial building under construction using C.F.S

2. Methodology

An experiment done by earlier studies [11, 12, 20, 22, 27, 29] includes 101 columns of tests, which were chosen for numerical and parametric study. These columns were numerically modeled using commercial F.E.A. software Abaqus®. Specimens considered cover the entire range of column slenderness ratio, Figure (6), in general construction, which is within the range (λ = 45-97) as per [28]. All details of experiments done with respect to the sources are reported in Table 1.

2.1. Numerical Modeling

Geometrical properties, post-fire material properties, and imperfections measured by [11-12, 20, 22, 27] were incorporated into numerical modelling. Sectional co-ordinates taken from the centerline of each cross-section were used to draw the specimen, following which the shell extrusion technique was used along the length using the GUI [30]. The general-purpose 4-node reduced integration shell element (S4R) is used with a square mesh size equal to the thickness of the section. Similar element types and sizes have proven efficient in determining steel column behavior [7-27]. The post-fire stress-strain curve mentioned in [11-12, 20, 22, 27] is an engineering stress-strain curve. This engineering stress-strain is converted into plastic true stress-strain using the equation $\sigma_{true} = \sigma_{eng.}(1+\varepsilon_{eng.})$, $\varepsilon_{true} = \varepsilon_{p} - [\mathrm{Ln}(\varepsilon_{eng.}+1)]$, where σ_{true}, $\sigma_{eng.}$, ε_{true}, and $\varepsilon_{eng.}$ are true and engineering

stress strain, ε_p is plastic strain. Thickness is assigned equally on either side of the centerline of cross-sections. Either end of the specimens was connected separately to a Reference Point (RP) using MPC constraints (Figure 5). The distance between the end face and the reference point is the distance between the axis of rotation and the end face of specimens [11-12, 20, 22, 27]. A simply supported boundary condition is given for all the columns, where the bottom end is restrained from translation and rotation in all directions except along the x-axis. A similar condition is provided at the top in addition to free translation along the y-axis for load application. Load is applied from the top (RP-2), Figure 5.

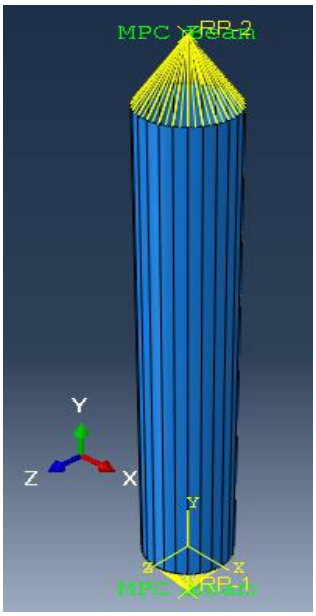

Fig. 5 Numerical modeling for validation

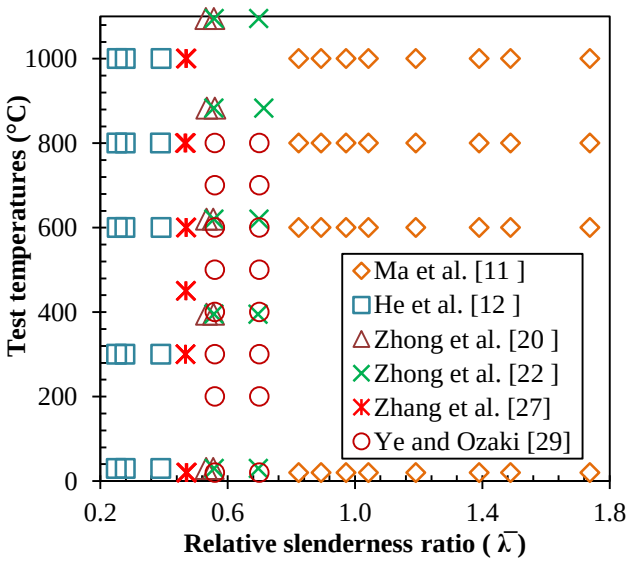

Fig. 6 Specimen temperature v/s slenderness ratio considered from the literature for validation

Further steps of loading and analysis are bifurcated into two stages. Stage-1 includes buckling analysis, and Stage-2 includes general static analysis with the effect of non-linear geometry and material properties. Initial buckling analysis is done with unit load (1 N) at the top reference point (RP-2, Figure 5, and a request to save the deformed shape is made in the model input file. Once the initial buckling analysis is done, the model is copied, and the buckling step is changed to a static general step by enabling Nlgeom (non-linear geometry and material). Once again, the input file is edited to induce the imperfection profile obtained in the form of mode shapes from the earlier buckling analysis.

Note that the mode shape with the least buckling load is adopted for global and local. Finally, analysis is continued, and failure load is taken as peak RF-2 from the bottom reference point (RP-1, Figure 5). A similar procedure is adopted for all the specimens [11-12, 20, 22, 27] by just changing geometrical and material properties with respect to the specimen under consideration. Note that residual stresses affect column capacities at room temperature. But at high temperatures, its effect is negligible.

Since the majority of the columns tested were at 600°C and above, residual stresses were not considered explicitly, except for room temperature specimens, which were adopted from [33]. In addition, note that global and local imperfections were measured and reported for all the specimens by [11-12, 20, 22], which were incorporated in the present study, except studies done by [27], which did not report imperfections; in such a case, limiting imperfection is adopted by standard [34] (global = L/1000, local B/100, where L = length of specimen, B = max. cross-section size).

2.2. Model Comparison and Validation

All numerical models were compared with experimental results, which include axial load vs. axial deformation, axial load vs. lateral deflection, and buckling loads. Some studies reported axial load vs. axial deformation [11, 29], whereas others reported axial load vs. lateral deflection [12, 20, 22, 27], but nevertheless, all studies tabulated buckling load in Table 1. Presently, validation of all 101 specimens is shown in Figure 14 and reported in Table 1. Some of the load vs. axial deformation is plotted in Figures 9 and 12, where two outputs from RP-1 (RF2) and RP-2 (U2) are shown.

Similarly, load vs. lateral deflection is plotted in Figures(7-8, 10-11), where two outputs from RP-1 (RF2) and (U3) from the node that has the highest lateral deflection (central height) are shown. All outputs were taken from the post-processing stage. All load vs. displacement/deformation are shown in Figures (7-12), with continuous lines representing experimental values and dotted lines representing F.E.A. values. Comparison shows good approximation with all the experiments, except minor

discrepancies among the comparison of Zhong et al. [20], Figure 10(b), and Ye and Ozaki [29], Figure 12(a). Various factors delineate the change between F.E.A. and experiments, such as unaccounted eccentricities, imperfections, and pin condition with friction. Discarding these factors in numerical modelling affects the stiffness of specimens. As stated earlier, Ye and Ozaki [29] did not measure geometrical imperfection for specimens with slenderness ratios of 40 and 50. Assumed geometrical imperfection of L/1000 as per [34] may have slightly influenced the stiffness and post-peak behavior of specimens in Figure 12(a). However, the present study mainly focuses on the capacity of columns rather than the axial or lateral stiffness. Having said that, all the validation comparisons plotted in Figures (7-12) have a good comparison of buckling load with minimal error.

Further comparison of F.E.A. and experiments is done in Figure 14. Since columns' relative slenderness ($\bar{\lambda}$) varied from 0.2 to 1.5, capacities too had a vast range. To normalize the capacities and plot them in a common frame, the ratios of $\sigma_{F.E.A}/\sigma_y$ and $\sigma_{Exp.}/\sigma_y$ are taken out. Where $\sigma_{F.E.A}$ and $\sigma_{Exp.}$ are the ratios of buckling load to area of specimen calculated separately for F.E.A and experiment, and σ_y is the yield stress of the column steel under consideration. If both the experiment and F.E.A. load match exactly, data points will lie on the continuous linear line shown in Figure 14. It should be noted that almost all (77%) of the data points in Figure 14 lie on the linear line with some minor exceptions (± 20%).

Similar to the graph, values mentioned in Table 1 also show a close mean (1.096) and C.O.V. (0.011). Supporting validity, failure modes of both F.E.A. and experiments done by [22] show a good approximation in Figure 13. Hence, by considering all the above factors, we can assume that the numerical model has been validated with experimental results.

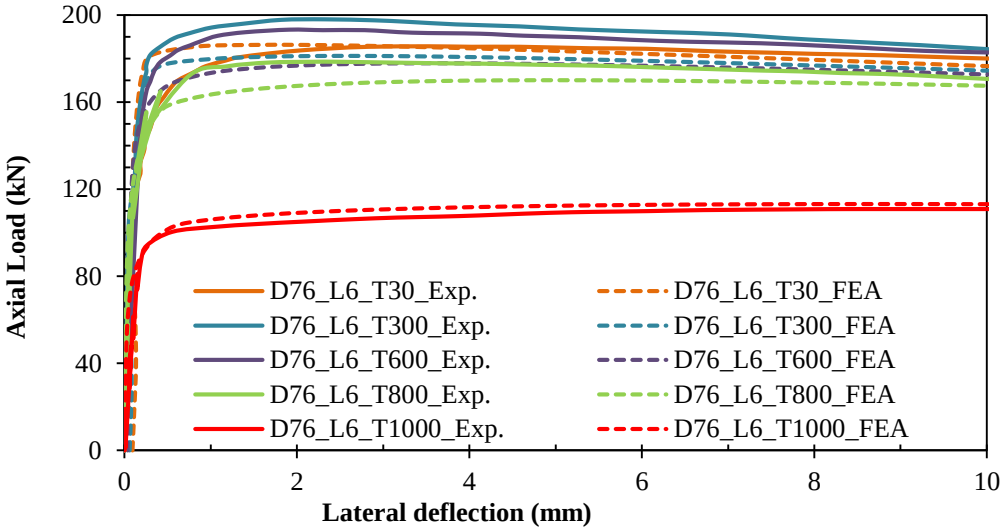

Fig. 7(a) Axial load v/s lateral deflection comparison [12]

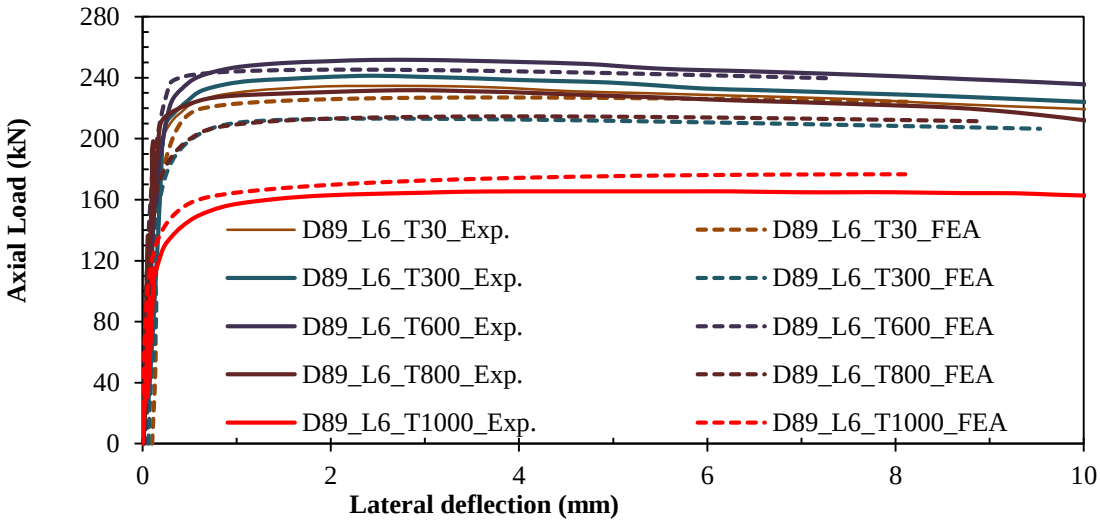

Fig. 7(b) Axial load v/s lateral deflection comparison [12]

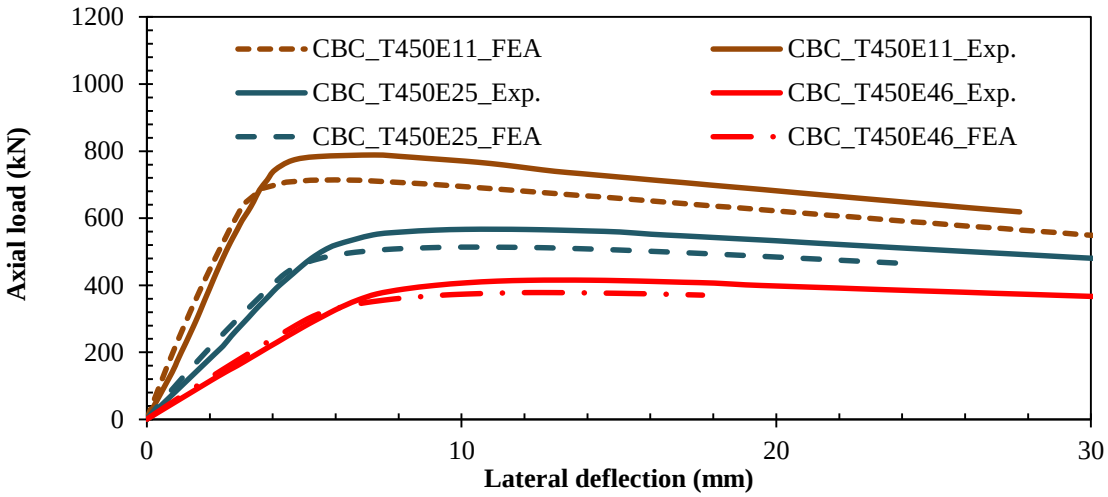

Fig. 8(a) Axial load v/s lateral deflection comparison [27]

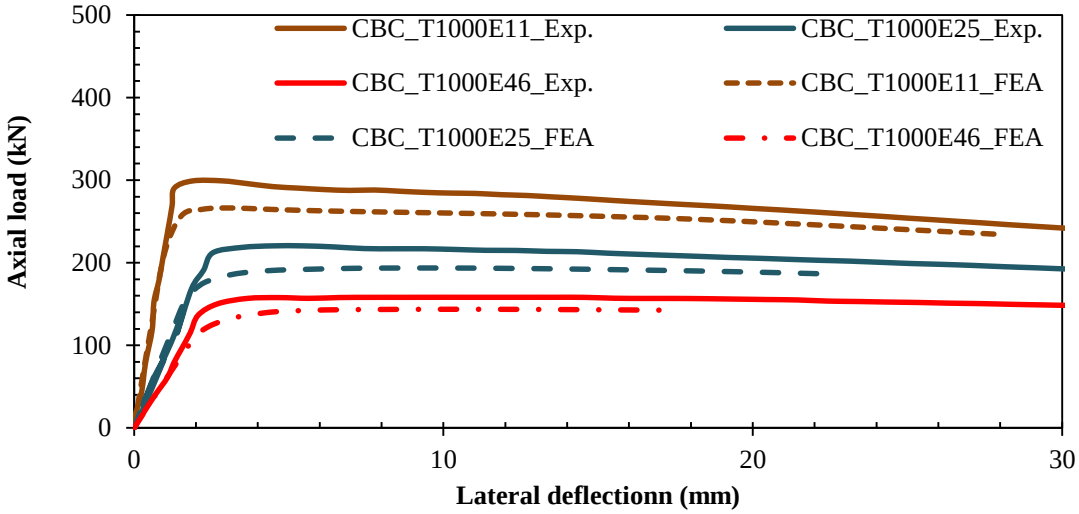

Fig. 8(b) Axial load v/s lateral deflection comparison [27]

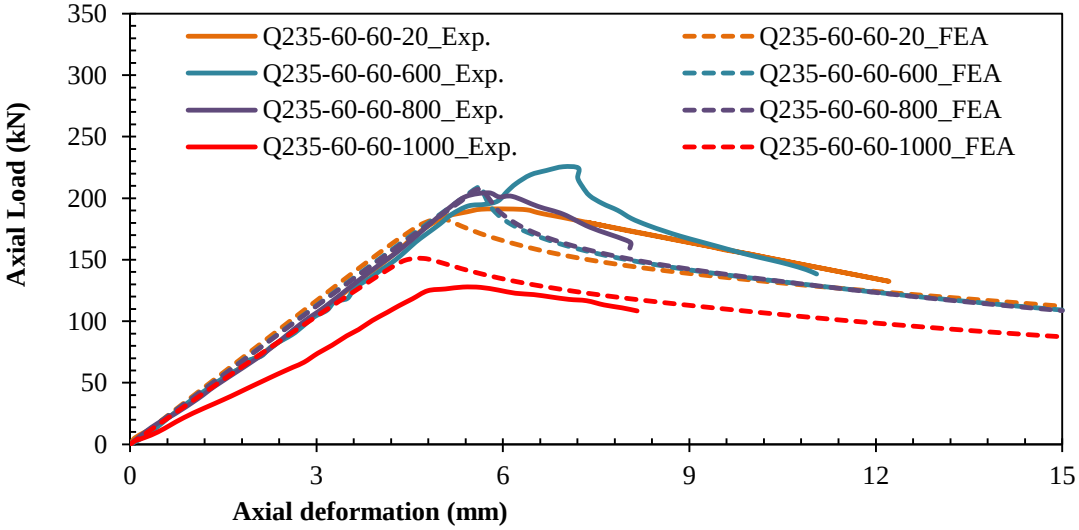

Fig. 9(a) Axial load v/s axial deformation comparison [11]

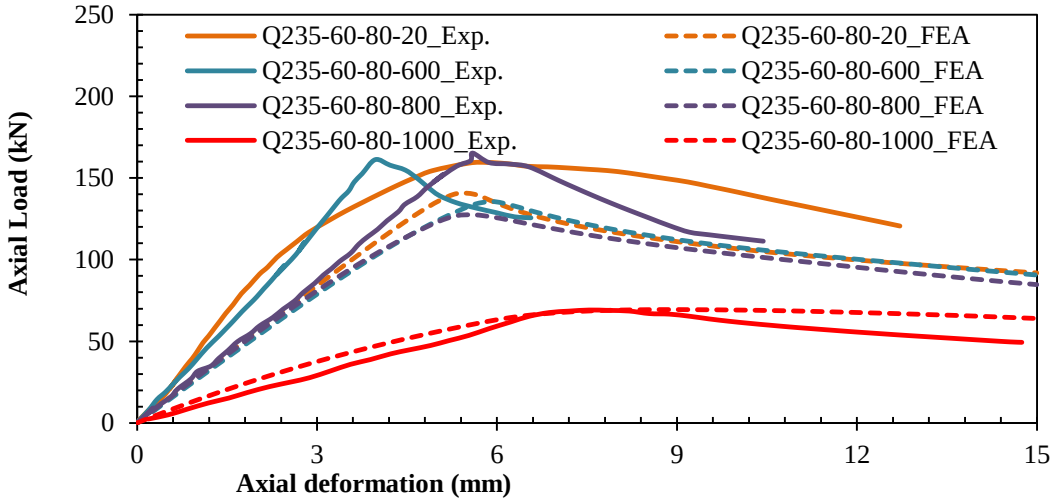

Fig. 9(b) Axial load v/s axial deformation comparison [11]

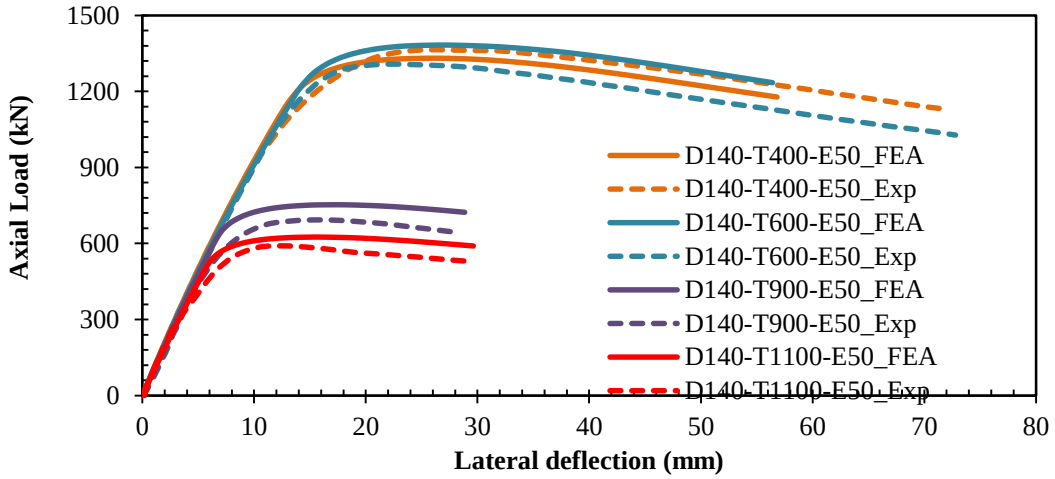

Fig. 10(a) Axial load v/s lateral deflection comparison [20]

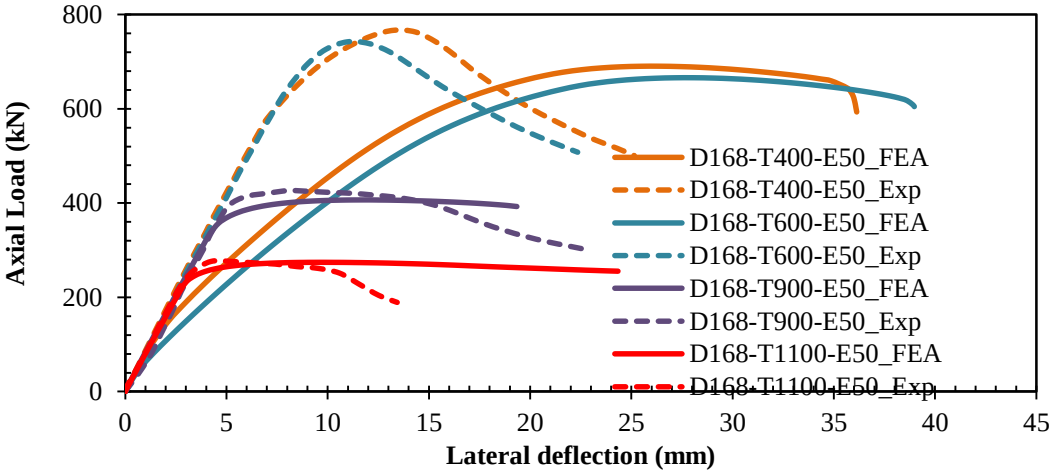

Fig. 10(b) Axial load v/s lateral deflection comparison [20]

3. Parametric Study

Among 101 validated models, various parameters such as temperature, eccentricities, and slenderness ratios were experimentally studied [7-27]. Twenty specimens that had a wide range of non-repeating slenderness ratios were selected for the parametric study (Table 3). Eccentricities ranging from 0 to 4Do (Do = Outer dia), were selected in Table 3.

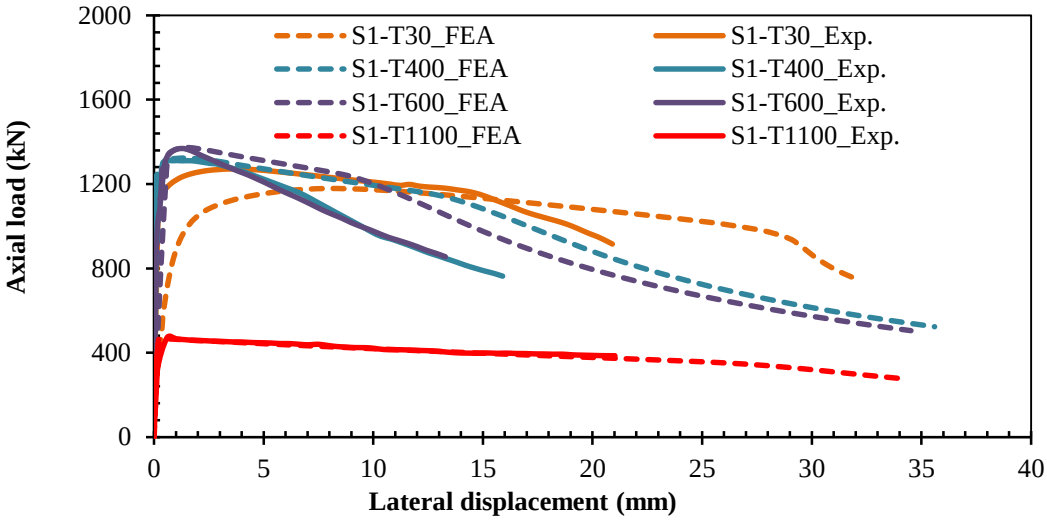

Fig. 11 (a) Axial load v/s lateral deflection comparison [22]

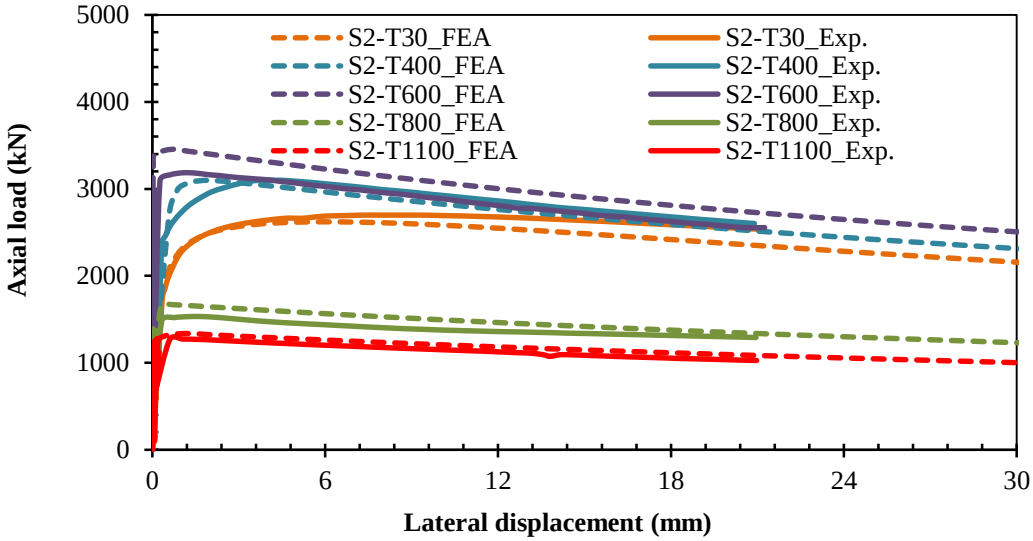

Fig. 11 (b) Axial load v/s lateral deflection comparison [22]

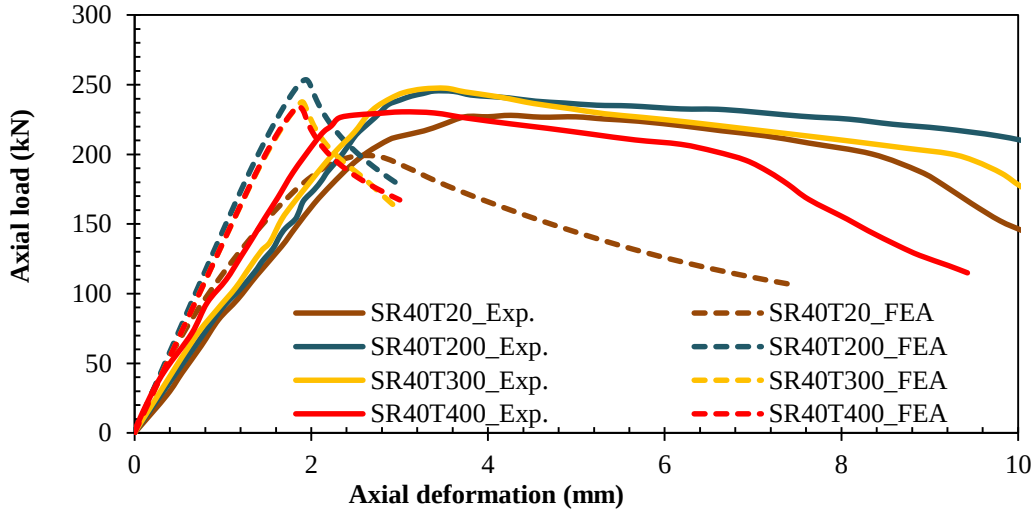

Fig. 12 (a) Axial load v/s axial deformation comparison [29]

This eccentricity range loads columns from pure bending to concentric axial loading. Three categories of temperature distributions were selected. 1. Unheated specimens, 2. Uniformly heated specimens, and 3. Specimens with realistic temperatures (parabolic), Figure 16 (b). These distributions help in dissecting the hidden effect of the heating regime.

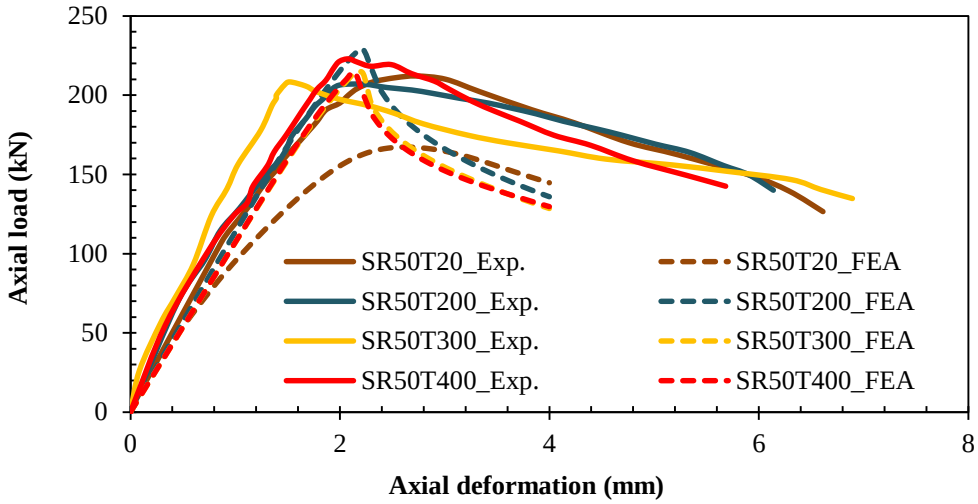

Fig. 12 (b) Axial load v/s axial deformation comparison [29]

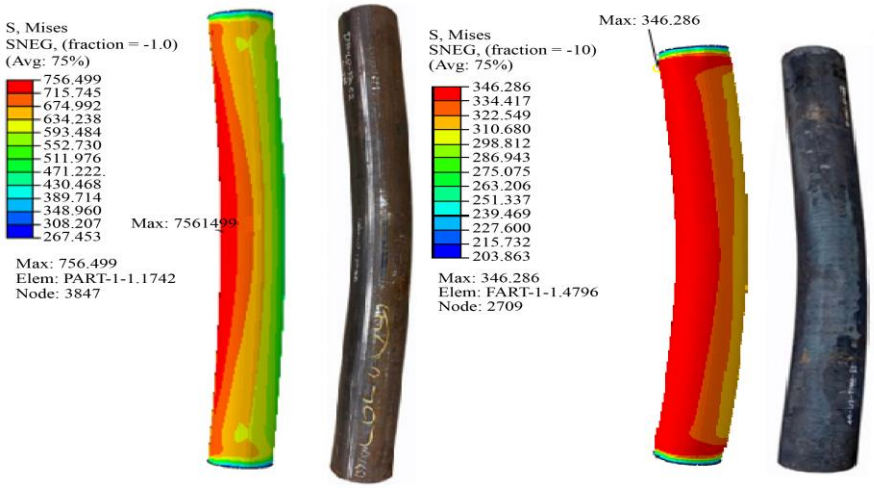

Fig. 13 Failure mode shapes of S2-T30 and S2-T1100 [22]

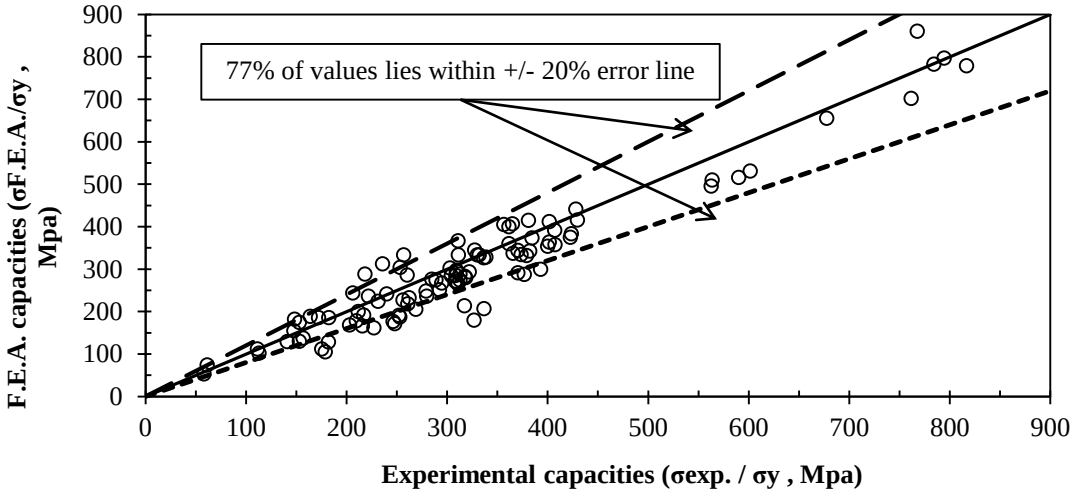

Fig. 14 Line of linearity, comparing the capacity of all specimens [11, 12, 20, 22, 27, 29]

A similar modelling procedure is explained in Section 2.1 and is adopted for modelling, except for two changes. Geometrical imperfections were limited to the tolerance specified by standards [34] intended for technical delivery conditions. As per [34], global imperfection of L/1000 and local imperfection of $D_o/100$ are used for all the models of Table 3. Another change is that common material property is assigned for all the columns as shown in Figure 15. Steel grade S275 [34] with yield 275 MPa and ultimate strength 410 MPa is used for all columns, as it is one of the common grades used in steel structures. Steel loses strength after being subjected to fire. The reduction of strength and material law given by [35] for Yst-310 steel is adopted and shown in Figure 15 and Table 2. Altogether 20 models with 6 types of eccentricities and three categories lead to 360 numerical trials, Table 3.

3.1. Realistic Temperature Distribution

As dealt with earlier, realistic temperature assumes nearly parabolic profiled heating. It can be assumed to have a peak temperature at 70% of column height and at the top 50% of the peak temperature, Figure 16(a). This non-uniform distribution of temperature can be fed to Abaqus® using a predefined field at the initial step, Figure 16(a). Instead of providing uniform distribution, spatial distribution using Equation (1) can be fed to an analytical field with a magnitude of 1000°C. Note that only the peak temperature of 1000°C is considered, as column capacity is critical at this temperature. Full-scale fire tests [2] showed that peak temperatures near 1000°C are quite common in buildings. Formulated temperature distribution with a peak at 0.7 h is shown in Figure 16(a). In addition, since all columns are symmetric about both axes, axisymmetric advantage is explored where half of the cross-section alone is modelled, and F.E.A. capacity is doubled for actual capacity, Figure 17(a). Note that the symmetric boundary condition is chosen in Abaqus® along the Y-axis in Figure 17(b).

$$x = -1.309y^3 - 0.839y^2 + 2.655y - 0.003 \quad (1)$$

3.2. Column Capacities Under Realistic Temperature Distribution

Steel columns lose up to 60% of their room temperature capacity at 1000°C [35]. This reduction affects both slender columns and columns with moments. Figures 18(a)-(c) show the effect of uniformly heated and realistically heated columns. In Figures 18(a)-(c), buckling loads from parametric analysis are converted to buckling stress ($\sigma_{F.E.A} = P_{F.E.A}/\text{Area}$) and expressed as ratios ($\sigma_{F.E.A} / \sigma_{y20}$, or $\sigma_{F.E.A} / \sigma_{y1000}$). Note that $\sigma_{y20} = 275$Mpa, and $\sigma_{y1000} = 103.7$ Mpa (as per Table 2). Resulting ratios are plotted in Figure 18(a)-(c), which shows that the buckling stress reduces as the slenderness ratio increases, showcasing P-Δ effects. Similarly, as the eccentricity increases, the load-carrying capacity decreases linearly as the moment affects the stability of the column. This linear distribution is proof that the interaction Equation (8) suggested by the European code [3] has a similar distribution. As the eccentricity increases, the majority of the strength goes into balancing the moment rather than the axial load; hence, higher eccentric columns (e=4D) have the least variation with respect to slenderness ratios, Figure 18 (a).

The line joining the y-axis at 1 indicates the line of yield strength; data values above this line are those specimens whose capacity exceeds the yield strength of the section. There is a greater difference between uniformly heated column capacities and realistically (parabolically) heated column capacities. This difference can be observed by comparing Figures 18(b) and (c), where the scattering for both figures is dissimilar. We can see that in Figure 18(c) column capacities exceed the line of yield for concentric columns (e=0), and mildly eccentric columns (e=0.25D) lie above 0.8 on the y-axis. Overall, we can conclude that realistically (parabolically) heated columns can sustain higher loads than uniformly heated columns. For concentric columns, a 40% increase in strength is observed, whereas for mildly eccentric columns (e=0.25D), up to a 30% increase in strength exists. Earlier studies on post-fire uniformly heated column capacities were estimated with good accuracy using standard code equations by mere replacement of room temperature yield strength with post-fire yield strength [10-27]. However, using such equations and models on realistically heated columns will result in excessive over-conservation. To overcome this setback, the next section deals with the formation of new equations and their accuracy in strength predictions.

4. Code Comparison

European code EN-1993-1-1 [3] provides column capacity under pure axial load with or without moments. Steel sections classified as four classes distinguish column capacities depending on plate slenderness. Class-1, 2, and 3 sections can undergo elastic moment before initiation of local buckling, but class-4 sections undergo local buckling even before the occurrence of elastic moment. The present parametric study consists mostly of class-1 sections; hence, the axial load and moment capacity given by EN-1993-1-1 [3] are described below. Note that for comparison, all partial safety factors are assumed to be 1 and $\alpha = 0.49$ for cold-formed sections as per EN-1993-1-1 [3]. In Equations (5)-(7), le = effective length, r_{min} = min. radius of gyration, E = Young's modulus, f_y = yield strength, W_{pl} = plastic section modulus. Interaction effect due to axial load and uni-axial moment must be less than or equal to 1, Equation (8), where N_{Ed} = ultimate load obtained by F.E.A, N_{EC} = design load as predicted by Equation (2) [3], $M_{z,Ed}$ = ultimate moment obtained by F.E.A, $M_{pl,EC}$ = design moment as predicted by [14] Equation (7), and Kzz = interaction factor as per Annex-B (method-2), given by Equation (9), where Cmz = 1 (for equal moments on either ends of columns)

$$N_{EC} = \chi A f_y \quad \text{for class 1, 2, and 3 cross-} \quad (2)$$

sections

$$\chi = \frac{1}{\phi \sqrt{\phi^2 - \bar{\lambda}^2}} \quad (3)$$

$$\phi = 0.5 [1+ \alpha (\bar{\lambda} - 0.2) + \bar{\lambda}^2) \quad (4)$$

$$\bar{\lambda} = (l_e / r_{min}) / (1 / \lambda_1) \quad (5)$$

$$\lambda_1 = \pi \sqrt{\frac{E}{f_y}} \quad (6)$$

$$M_{pl.Ec} = W_{pl} * f_y \quad (7)$$

$$\frac{N_{Ed}}{N_{EC}} + k_{zz} \frac{M_{z,Ed}}{M_{pl,EC}} \leq 1 \quad (8)$$

$$k_{zz} = C_{mz} \left[1 + (\bar{\lambda} - 0.2) \frac{N_{EC}}{\chi N_{Ed}}\right] \leq C_{mz} \left[1 + 0.8 \frac{N_{EC}}{\chi N_{Ed}}\right] \quad (9)$$

All 360 numerical capacities obtained by the parametric study were compared with code capacity predictions. Note that for the three cases considered, the procedure used for determining capacity remained the same, except for yield strength, which is 275 MPa for unheated specimens, 103.7 MPa for uniformly heated specimens, and specimens with realistic temperatures (parabolic). All comparisons are plotted in Figure 19(a)-(c). All predictions of unheated capacities predicted by the European code [3] lie on the safer side with slight conservation 19(a). Heated specimens' predictions were scattered 19(b) as compared to unheated specimens' 19(a). The primary reason for this is that for unheated columns, the room temperature (Abaqus®) stress-strain is without substantial strain hardening (Figure 15), whereas for post-heated specimens, stress-strain input was complex, and after 300°C, stress-strain had higher strain hardening (Figure 15). Such a distribution was suggested by the material model of [35]. Secondly, unlike axially loaded columns, where strains remain within the plastic region of the stress-strain curve, eccentrically loaded columns' strains reach the strain hardening region after specific plastic straining (Figure 15). For the entire calculation of strength and interaction from the European code, Equations (2)-(9), yield strength is used as a strength criterion, whereas an eccentrically loaded column can even reach ultimate strength under pure bending at extreme eccentricity (e = 4Do). These are the main reasons for the over-conservative and scattered prediction of column capacities by code Figures 19(b-c). However, keeping all other factors similar, there exists extreme conservation and scattering in Figure 19(c), as compared to Figure 19(b). This shows that additional capacity and moment can be taken by columns with a realistic temperature distribution. Hence, conventional code capacity equations (Equations (2)-(9) of [3]) are not sufficient to determine column capacities, so the next section deals with framing a separate capacity equation for it.

4.1. Capacity Formulation for Realistic Fire Scenario

To this end, we have seen the importance of considering non-uniform or realistic temperature distribution in the capacity assessment of columns. To determine the capacity of columns in such a case, we need to mathematically assess the difference in heat energy between uniformly heated and realistically heated columns. Consider a column of length L heated by two different profiles, as shown in Figure 20. Keeping all other factors constant, the area under profile A and profile B is analogous to the heat energy of the respective columns.

Due to the similar length of both columns, it can be equated to unity (1). Area under the curve, which is B, can be obtained by integrating Eq.1 within the limit 0 to 1, Equation (10). After integration, the area under the curve B is 0.7177. Similarly, the area under a uniformly heated column is 1 x 1 = 1. Now, to obtain how many parabolic profiles can be fit into uniformly heated columns, we can divide 1/0.717, which equals 1.393. Practically, it is the indication that columns under realistic fires can withstand 1.393 or ≈1.4 times more axial load than the uniformly heated columns. Hence, Equations (2) and (8) can be rewritten as Equations (11) and (12), where $N_{EC, R}$ = revised column capacity. Note that the factor 1.393 can only be multiplied by N_{EC}, but not for $M_{pl, EC}$, this is because, as we observe N_{EC}, it accounts for geometrical stability since it depends on length (slenderness ratio), whereas $M_{pl,EC}$ depends completely on cross-sectional area without influence of column length. Hence, since variation of temperature is considered along column length only, N_{EC} needs to be revised with $N_{EC, R}$. If there is any cross-sectional temperature change, it will have an influence on both N_{EC} and $M_{pl, EC}$. Further, such variation from practical heating is under process and will be presented in future studies. All calculated capacities using revised Equations (11) and (12) are plotted in Figure 21. It can be noted that dispersion and accuracy have been increased in comparison to Figure 21. Further validity of the revised equation can be evidenced using the mean and standard deviation from Table 4. Proposed equations provided a mean and S.D. of 1.425 and 0.452, which is lower than 2.183 and 0.7063, which resulted from Equations (11) and (12). Hence, by observing the accuracy of the proposed equation and safe prediction from Figure 21, we can conclude that Equations (11) and (12) can be safely used to determine the post-fire load-carrying capacity of a steel column. Additionally, standards such as the American specification [4] and the Australian standard [5] use a similar approach to that of the European code [3] with minor changes. Hence, by merely multiplying the coefficient (1.393) by the axial load prediction equation, we can obtain column capacities for a realistic temperature distribution.

$$\int_0^1 x = \int_0^1 (-1.309y3 - 0.839y2 + 2.655y - 0.003)\, dx \quad (10)$$

$$= 0.717715$$

$$= 1 / 0.717$$

$$= 1.393$$

$$N_{EC,R} = (\chi A f_y) * 1.393 \quad (11)$$

$$\frac{N_{Ed}}{N_{EC,R}} + k_{zz}\frac{M_{z,Ed}}{M_{pl,EC}} \leq 1 \quad (12)$$

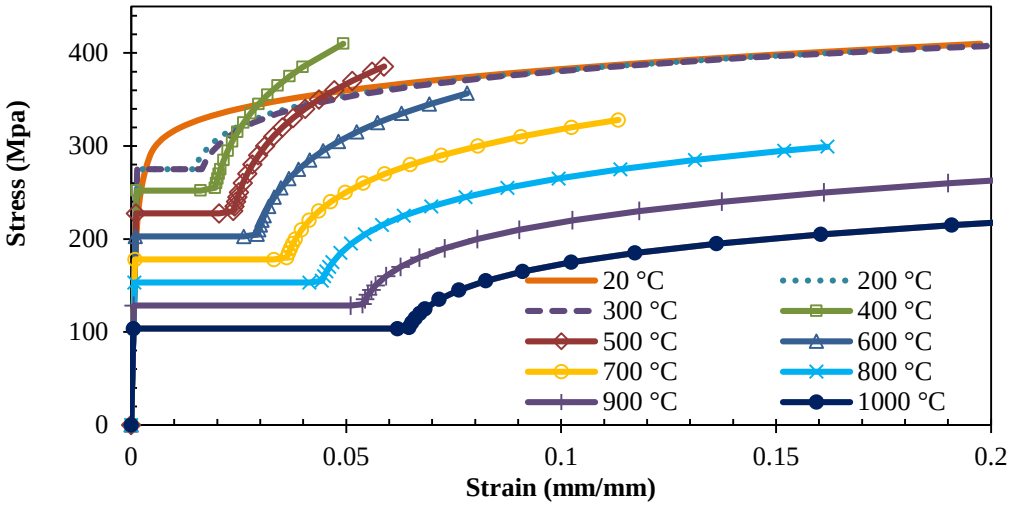

Fig. 15 Post-fire stress-strain model for parametric study, computed using Table 2 [35]

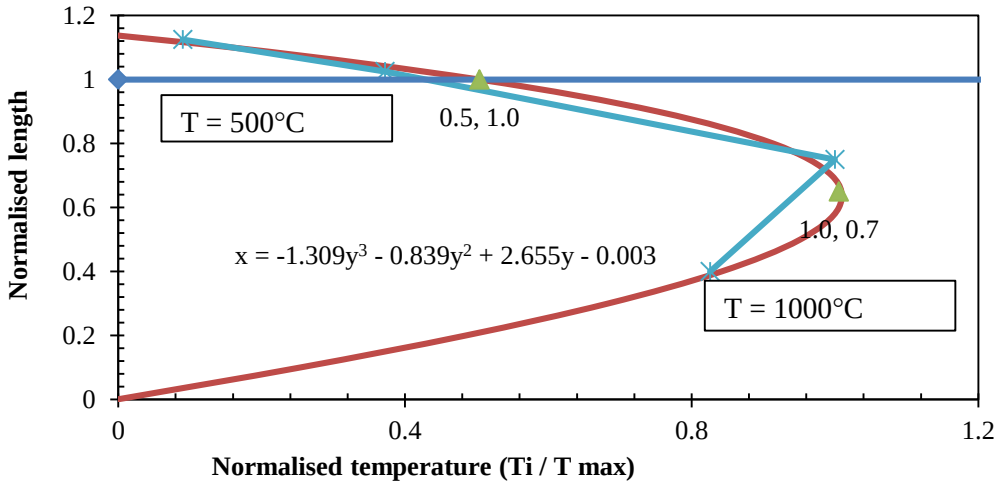

Fig. 16(a) Realistic temperature distribution adopted for parametric study

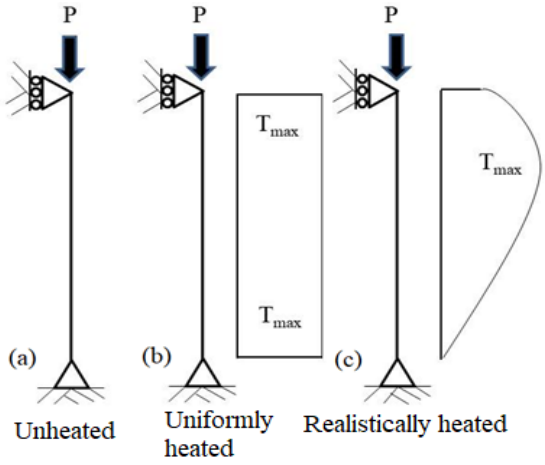

Fig. 16(b) Three cases considered for parametric study

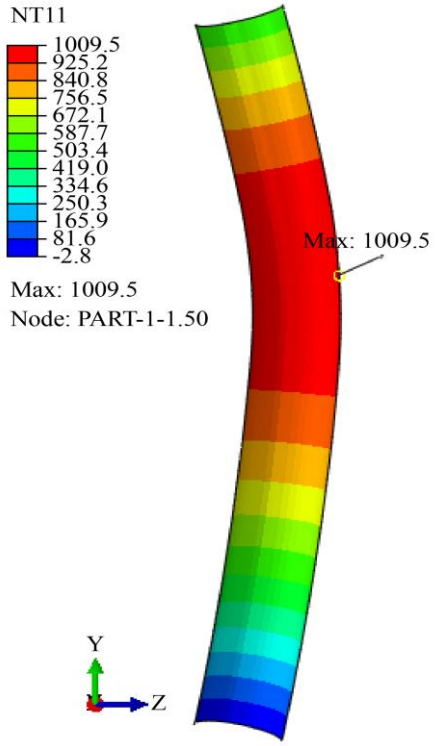

Fig. 17(a) Temperature distribution of F.E.A model (parametric study)

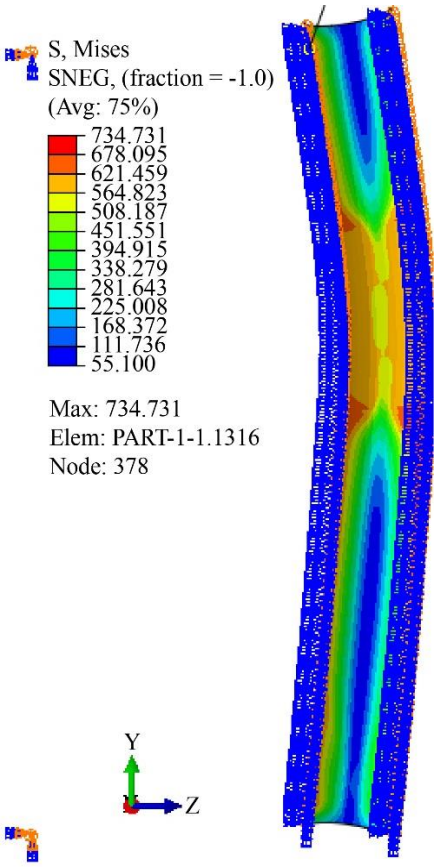

Fig. 17(b) Symmetric boundary condition with stress distribution at peak load (parametric study)

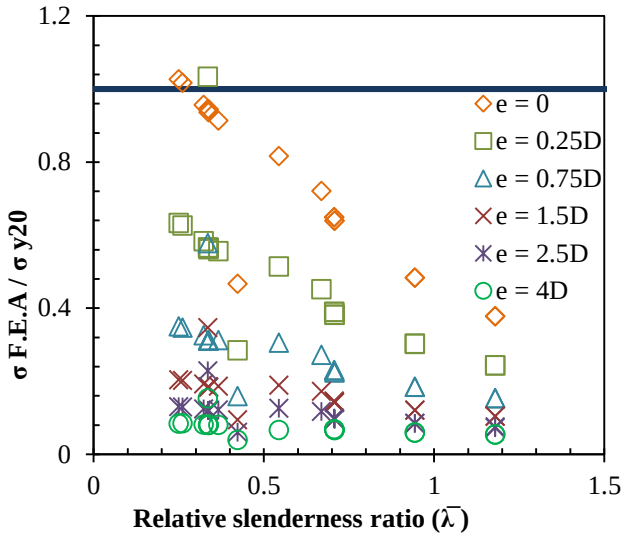

Fig. 18(a) Unheated column capacities

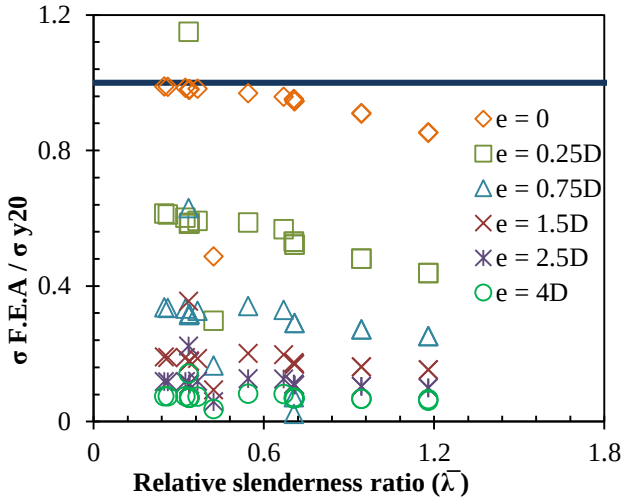

Fig. 18(b) Fully heated column capacities

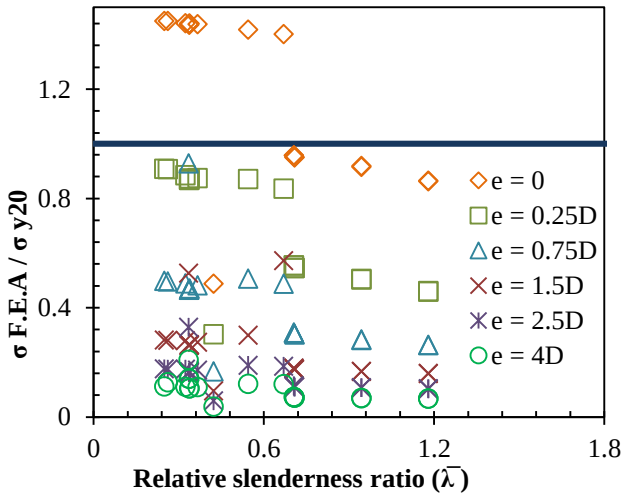

Fig. 18(c) Realistically heated column capacities

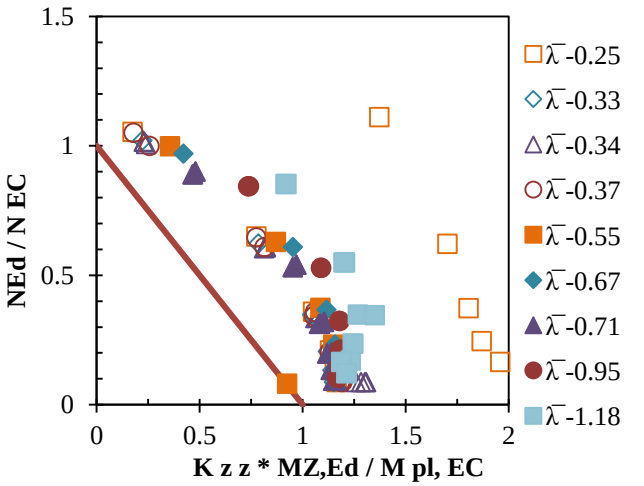

Fig. 19(a) Unheated column capacity interaction from Equation (8) [3]

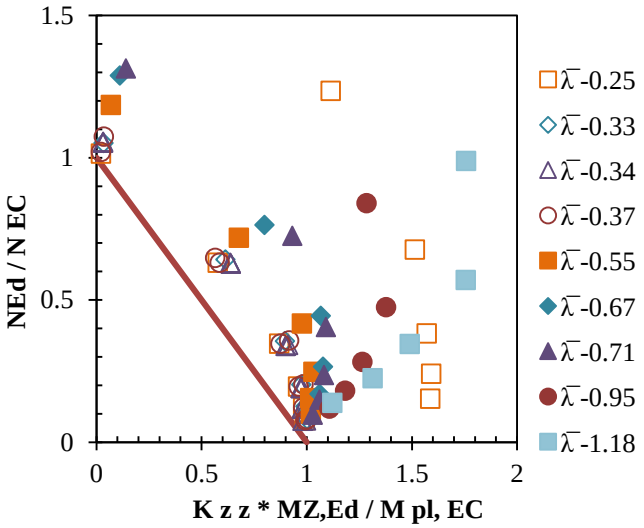

Fig. 19(b) Uniformly heated column capacity interaction from Equation (8) [3]

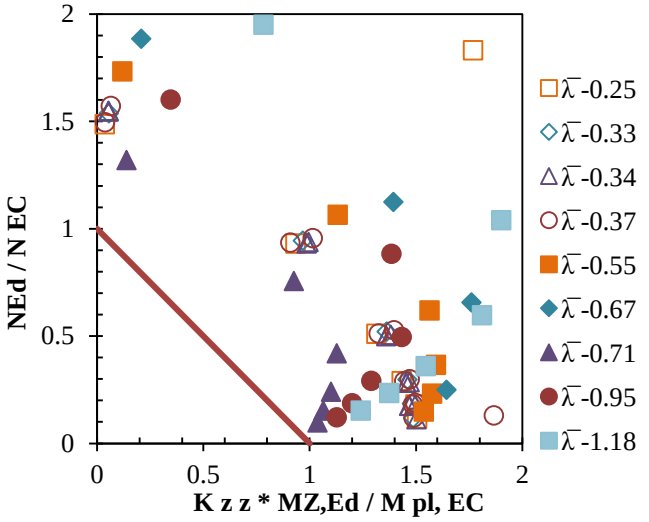

Fig. 19(c) Realistically heated column capacity interaction from Equation (8) [3]

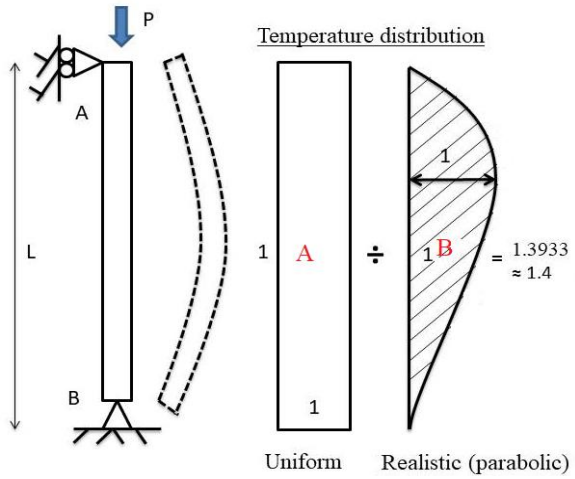

Fig. 20 Mathematical model to determine heat energy distribution

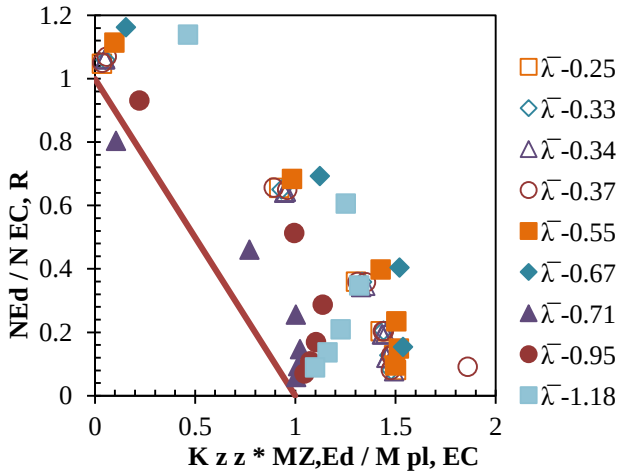

Fig. 21 Proposed model capacity comparison for realistic temperature distribution from revised equation Equation (13)

5. Conclusion

The present study dealt with the capacity estimation of steel columns under realistic temperature distribution. Altogether 101 validated numerical models using Abaqus® were used to assess the effect of realistic temperature distribution over uniform temperature idealization. The modelling procedure and efficient parameters used are explained in detail. A parametric study of 360 numerical trials was analyzed to revise the Eurocode capacity equations.

The critical outcome of the present study is listed below.

- Realistically, heated columns can sustain up to 40% more axial load than uniformly heated columns; this increase is 30% for eccentric columns.
- The conventional design equation from the European code greatly underestimates realistically heated column capacities.
- The capacity equations are developed by analysing the differences in heat energy required for the two distribution regimes.
- Formulated equations provide a more accurate prediction of realistically heated column capacities as

compared to the European code equations.

- Evaluated capacity equations can be safely used to determine the residual strength of a steel column subjected to a realistic temperature distribution.

Data statement

All data used in the present study are available on request.

Author's Contribution

Rakshith B. D – Conceptualization, Methodology, Software, Validation, Formal analysis, Investigation, Writing - Original draft, Visualisation, supervision.

Punitha kumar A. – Supervision, Writing – review and editing, Project administration, Resources.

References

[1] Yusuke Shintani et al., "Experimental Investigation of Burning Behavior of Automobiles," *6th Asia-Oceania Symposium on Fire Science and Technology*, Daegu, Korea, pp. 1-13, 2004. [Google Scholar] [Publisher Link]

[2] B.R. Kirby, The Behaviour of a Multi-Storey Steel Framed Building Subjected to Fire Attack: Experimental Data, Swinden Technology Center World Beaters in Applied Steel Research, 1998. [Online]. Available: https://www.steelconstruction.info/File:Behaviour_Multi_Storey_Steel_Framed_Building_Subject_to_Fire_Attack_-_Experimental_data.pdf

[3] EN 1993-1-1:2005, Eurocode 3: Design of Steel Structures - Part 1-1: General Rules and Rules of Buildings, 2005. [Online]. Available: https://www.phd.eng.br/wp-content/uploads/2015/12/en.1993.1.1.2005.pdf

[4] Specification for Structural Steel Buildings (ANSI/AISC 360-22), American Institute of Steel Construction (AISC), 2022. [online]. Available: https://www.aisc.org/Specification-for-Structural-Steel-Buildings-ANSIAISC-360-22-Download

[5] AS4100:2020, Steel Structures, Standards Catalogue, Standards Australia, 2020. [Online]. Available: https://www.standards.org.au/standards-catalogue/standard-details?designation=as-4100-2020

[6] The Sustainable Development Goals Report 2025, Sustainable Development Goals, United Nations, 2025. [Online]. Available: https://unstats.un.org/sdgs/report/2025

[7] Wei Ji et al., "Experimental and Numerical Study on Fire-Induced Collapse of Double-Span Steel Portal Frames," *Fire Safety Journal*, vol. 143, 2024. [CrossRef] [Google Scholar] [Publisher Link]

[8] Weiyong Wang, and Tianzi Liu, "Experimental and Numerical Study on Post-Fire Behavior of High-Strength Q460 Steel Columns," *Advances in Structural Engineering*, vol. 19, no. 12, pp. 1873-1888, 2016. [CrossRef] [Google Scholar] [Publisher Link]

[9] ISO 834-1:1999, Fire-Resistance Tests-Elements of Building Construction, Part 1-General Requirements, International Organization of Standards, 1999. [Online]. Available: https://www.iso.org/standard/2576.html

[10] Shaohua Han, Yu Chen, and Wentao Xie, "Behavior of Square Hollow Steel Tubular (SHST) Stub Columns after Elevated Temperature," *Journal of Constructional Steel Research*, vol. 136, pp. 177-192, 2017. [CrossRef] [Google Scholar] [Publisher Link]

[11] Riu Ma, Hongbo Liu, and Zhihua Chen, "Calculation Method for the Residual Stability Bearing Capacity Under Axial Compression of Steel Tube Members Exposed to a High Tempareature," *Thin-Walled Structures*, vol. 132, pp. 475-493, 2018. [CrossRef] [Google Scholar] [Publisher Link]

[12] An He et al., "Flexural Buckling Behavior and Residual Strengths of Stainless Steel CHS Columns after Exposure to Fire," *Thin-Walled Structures*, vol. 152, pp. 1-40, 2020. [CrossRef] [Google Scholar] [Publisher Link]

[13] An He, Yating Liang, and Ou Zhao, "Experimental and Numerical Studies of Austenitic Stainless Steel CHS Stub Columns after Exposed to Elevated Temperatures," *Journal of Constructional Steel Research*, vol. 154, pp. 293-305, 2019. [CrossRef] [Google Scholar] [Publisher Link]

[14] Kang He, Yu Chen, and Shaohua Han, "Experimental Investigation of Square Stainless Steel Tubular Stub Columns after Elevated Temperatures," *Journal of Constructional Steel Research*, vol. 159, pp. 397-414, 2019. [CrossRef] [Google Scholar] [Publisher Link]

[15] Guo-Qiang Li et al., "Investigation on Postfire Residual Capacity of High-Strength Steel Columns with Axial Restraints," *Journal of Structural Engineering*, vol. 146, no. 9, 2020. [CrossRef] [Google Scholar] [Publisher Link]

[16] Yukai Zhong et al., "Post-Fire Behaviour and Residual Resistances of S700 High Strength Steel Tubular Section Stub Column Under Combined Loading," *Thin-Walled Structures*, vol. 169, 2021. [CrossRef] [Google Scholar] [Publisher Link]

[17] Yukai Zhong, Kang Hai Tan, and Ou Zhao, "Experimental and Numerical Investigation of S700 High Strength Steel Tubular Section Stub Columns after Exposure to Elevated Temperatures," *Thin-Walled Structures*, vol. 163, 2021. [CrossRef] [Google Scholar] [Publisher Link]

[18] Andi Su et al., "Post-Fire Behavior and Resistance of S690 High Steel Welded I-Section Stub Columns," *Thin-Walled Structures*, vol. 169, 2021. [CrossRef] [Google Scholar] [Publisher Link]

[19] Andi Su et al., "Experimental and Numerical Investigation into S960 Ultra-High Strength Steel Welded I-Section Stub Columns after Exposure to Elevated Temperatures," *Thin-Walled Structures*, vol. 183, 2023. [CrossRef] [Google Scholar] [Publisher Link]

[20] Yukai Zhong, Ou Zhao, and Leroy Gardner, "Experimental and Numerical Investigation of S700 High Strength Steel CHS Beam-Columns After Exposure to Fire," *Thin-Walled Structures*, vol. 175, pp. 1-42, 2022. [CrossRef] [Google Scholar] [Publisher Link]

[21] Yukai Zhong, and Ou Zhao, "Experimental and Numerical Studies on Post-Fire Behavior of S700 High Strength Steel Circular Hollow Sections Under Combined Compression and Bending," *Thin-Walled Structures*, vol. 181, 2022. [CrossRef] [Google Scholar] [Publisher Link]

[22] Yukai Zhong et al., "Structural Response and Residual Capacity of S700 High-Strength Steel CHS Columns after Exposure to Elevated Temperatures," *Journal of Structural Engineering*, vol. 148, no. 6, 2022. [CrossRef] [Google Scholar] [Publisher Link]

[23] Yukai Zhong, Andi Su, and Ou Zhao, "Post-Fire Local Buckling Behavior of Cold-Formed S700 High Strength Steel Circular Hollow Sections Under Axial Compression: Experiments, Modeling and Design," *Thin-Walled Structures*, vol. 184, 2023. [CrossRef] [Google Scholar] [Publisher Link]

[24] Wenkang Zuo, Man-Tai Chen, and Ben Young, "Structural Behavior of Cold-Formed Steel Elliptical Hollow Section Stub Columns after Exposure to ISO-834 Fire Curve," *Thin-Walled Structures*, vol. 197, 2024. [CrossRef] [Google Scholar] [Publisher Link]

[25] Wenkang Zuo, Man-Tai Chen, and Ben Young, "Post-Fire Behavior of Cold-Formed Steel Semi-Oval Hollow Stub Columns," *Journal of Structural Engineering*, vol. 150, no. 10, 2024. [CrossRef] [Google Scholar] [Publisher Link]

[26] Weiyong Wang et al., "Experimental and Numerical Study on the Behavior of High Strength Q960 Steel Columns after Fire Exposure," *Thin-Walled Structures*, vol. 198, 2024. [CrossRef] [Google Scholar] [Publisher Link]

[27] Jiahao Zhang, Hua Yang, and Andi Su, "Post-Fire Behavior and Resistance of S890 Ultra-High Strength Steel Circular Hollow Section Beam-Columns," *Thin-Walled Structures*, vol. 204, 2024. [CrossRef] [Google Scholar] [Publisher Link]

[28] Kang-Hai Tan et al., "Structural Response of Restrained Steel Columns at Elevated Temperatures. Part-1: Experiments," *Engineering Structures*, vol. 29, no. 8, pp. 1641-1652, 2007. [CrossRef] [Google Scholar] [Publisher Link]

[29] Kai Ye, and Fuminobu Ozaki, "Post-Fire Mechanical Properties and Buckling Strength of Cold-Formed Steel Hollow Section Columns," *Journal of Constructional Steel Research*, vol. 184, 2021. [CrossRef] [Google Scholar] [Publisher Link]

[30] Karlsson Hibbitt, and Inc Sorensen, "ABAQUS/Standard User's Manual Volumes I-III and ABAQUS CAE Manual," *SIMULIA, Providence*, RI, USA, 2014. [Google Scholar]

[31] Lin-Xin Song et al., "Experimental Study on the Effects of Whole Heating Cycle on Post-Fire Behavior of Restrained High Strength Structural Steel Columns," *Journal of Building Engineering*, vol. 70, 2023. [CrossRef] [Google Scholar] [Publisher Link]

[32] Jiahao Zhang, Andi Su, and Ke Jiang, "Post-Fire Behavior and Residual Resistance of S890 Ultra-High Strength Steel Circular Hollow Sections Under Combined Compression and Bending," *Engineering Structures*, vol. 316, 2024. [CrossRef] [Google Scholar] [Publisher Link]

[33] Jia-Lin Ma, Tak-Ming Chan, and Ben Young, "Material Properties and Residual Stresses of Cold-Formed High-Strength-Steel Circular Hollow Sections," *Journal of Constructional Steel Research*, vol. 109, pp. 152-165, 2015. [CrossRef] [Google Scholar] [Publisher Link]

[34] BS EN 10219-2:2006, Cold Formed Welded Structural Hollow Sections of Non-Alloy and Fine Grain Steels-Part-2: Tolerances, Dimensions and Sectional Properties, British Standards Institution, 2006. [Online]. Available: https://knowledge.bsigroup.com/products/cold-formed-welded-structural-hollow-sections-of-non-alloy-and-fine-grain-steels-tolerances-dimensions-and-sectional-properties

[35] Tekcham Gishan Singh, and Konjengbam Darunkumar Singh, "Post-Fire Mechanical Properties of Yst-310 Cold-Formed Steel Tubular Sections," *Journal of Constructional Steel Research*, vol. 153, pp. 654-666, 2019. [CrossRef] [Google Scholar] [Publisher Link]

[36] EN 10219-1: 2006, Cold Formed Welded Structural Hollow Sections of Non-Alloy and Fine Grain Steels-Part-1: Technical Delivery Conditions, Brussels: European Committee for Standardization; 2006. [Online]. Available: https://www.botopsteelpipes.com/wp-content/uploads/2024/08/EN-10219-1-2006.pdf

Appendix

Table 1. Details of experimental specimens considered for validation

Sl.No.	Author-s	Specimen Name	Yield strength (f_{yt})	$\bar{\lambda}_{20}$	Load type	Temp (°C)	Exp. Load (kN)	F.E.A Load (kN)	$P_{exp.}/P_{F.E.A.}$
1	An He et al. (2020) [12]	D73-L6-T30	303 (SS)	0.28	Axial	30	186	186	1.00
2		D73-L6-T300	290 (SS)	0.28	Axial	300	198	181	1.10
3		D73-L6-T600	287 (SS)	0.28	Axial	581	193	178	1.09
4		D73-L6-T800	262 (SS)	0.28	Axial	804	179	170	1.05
5		D73-L6-T1000	177 (SS)	0.28	Axial	1007	111	113	0.98
6		D73-L9-T30	303 (SS)	0.39	Axial	30	187	175	1.07
7		D73-L9-T300	290 (SS)	0.39	Axial	300	187	165	1.13
8		D73-L9-T600	287 (SS)	0.39	Axial	581	190	162	1.17
9		D73-L9-T800	262 (SS)	0.39	Axial	804	171	152	1.12
10		D73-L9-T1000	177 (SS)	0.39	Axial	1007	123	103	1.20
11		D89-L6-T30	292 (SS)	0.25	Axial	30	235	227	1.04
12		D89-L6-T300	288 (SS)	0.25	Axial	300	241	212	1.14
13		D89-L6-T600	323 (SS)	0.25	Axial	581	252	245	1.03
14		D89-L6-T800	284 (SS)	0.25	Axial	804	232	215	1.08
15		D89-L6-T1000	215 (SS)	0.25	Axial	1007	166	177	0.94
16	Zhang et al. (2024) [27]	CBC-T20-E11.1	893.4	0.61	Axial + Ec.	20	815	713	1.14
17		CBC-T20-E25.9	893.4	0.60	Axial + Ec.	20	590	524	1.13
18		CBC-T20-E46.3	893.4	0.61	Axial + Ec.	20	435	381	1.14
19		CBC-T300-E11.1	902.0	0.60	Axial + Ec.	300	849	750	1.13
20		CBC-T300-E25.9	902.0	0.60	Axial + Ec.	300	592	535	1.11
21		CBC-T300-E46.3	902.0	0.60	Axial + Ec.	300	452	402	1.12
22		CBC-T450-E11.1	845.1	0.60	Axial + Ec.	450	789	714	1.10
23		CBC-T450-E25.9	845.1	0.60	Axial + Ec.	450	567	514	1.10
24		CBC-T450-E46.3	845.1	0.60	Axial + Ec.	450	416	378	1.10
25		CBC-T600-E11.1	847.9	0.60	Axial + Ec.	600	789	695	1.13
26		CBC-T600-E25.9	847.9	0.60	Axial + Ec.	600	560	496	1.13
27		CBC-T600-E46.3	847.9	0.60	Axial + Ec.	600	405	349	1.16
28		CBC-T800-E11.1	352.2	0.60	Axial + Ec.	800	396	335	1.18
29		CBC-T800-E25.9	352.2	0.60	Axial + Ec.	800	297	253	1.18
30		CBC-T800-E46.3	352.2	0.60	Axial + Ec.	800	217	184	1.18
31		CBC-T1000-E11.1	293.6	0.61	Axial + Ec.	1000	301	266	1.13
32		CBC-T1000-E25.9	293.6	0.60	Axial + Ec.	1000	221	194	1.14
33		CBC-T1000-E46.3	293.6	0.60	Axial + Ec.	1000	159	144	1.11
34	Riu Ma et al. (2018) [11]	Q235-60-60	438	0.89	Axial	20	192	184	1.05
35		Q235-60-60	436	0.89	Axial	563	227	210	1.08
36		Q235-60-60	387	0.89	Axial	790	205	207	0.99
37		Q235-60-60	364	0.89	Axial	972	128	151	0.85
38		Q235-60-80	438	1.19	Axial	20	159	141	1.13
39		Q235-60-80	436	1.19	Axial	563	162	136	1.19
40		Q235-60-80	387	1.19	Axial	790	167	128	1.31
41		Q235-60-80	364	1.19	Axial	972	69	69	0.99
42		Q235-60-100	438	1.49	Axial	20	134	103	1.30
43		Q235-60-100	436	1.49	Axial	563	141	101	1.40

Table 2. Details of experimental specimens considered for validation (continued)

Sl.No.	Author-s	Specimen Name	Yield strength (f_{yt})	$\bar{\lambda}_{20}$	Load type	Temp. (°C)	Exp. Load (kN)	F.E.A Load (kN)	$P_{exp.}/P_{F.E.A.}$
44	Riu Ma et al. (2018) [11]	Q235-60-100	387	1.49	Axial	790	95	109	0.87
45		Q235-60-100	364	1.49	Axial	972	38	46	0.82
46		Q235-89-60	383	0.82	Axial	20	270	200	1.35
47		Q235-89-60	382	0.82	Axial	563	256	258	0.99
48		Q235-89-60	326	0.82	Axial	790	247	240	1.03
49		Q235-89-60	325	0.82	Axial	972	175	202	0.87
50		Q345-60-60	444	0.91	Axial	20	244	186	1.31
51		Q345-60-60	457	0.91	Axial	563	253	222	1.14
52		Q345-60-60	391	0.91	Axial	790	234	178	1.31
53		Q345-60-60	333	0.91	Axial	972	92	113	0.81
54		Q345-60-80	444	1.21	Axial	20	209	129	1.63
55		Q345-60-80	457	1.21	Axial	563	197	133	1.48
56		Q345-60-80	391	1.21	Axial	790	203	112	1.82
57		Q345-60-80	333	1.21	Axial	972	111	65	1.70
58		Q345-60-100	444	1.52	Axial	20	153	110	1.39
59		Q345-60-100	457	1.52	Axial	563	154	107	1.44
60		Q345-60-100	391	1.52	Axial	790	113	80	1.42
61		Q345-60-100	333	1.52	Axial	972	36	33	1.08
62		Q345-89-60	400	0.86	Axial	20	280	249	1.13
63		Q345-89-60	394	0.86	Axial	563	278	306	0.91
64		Q345-89-60	312	0.86	Axial	790	269	204	1.32
65		Q345-89-60	270	0.86	Axial	972	187	119	1.57
66	Zhang et al. (2024) [27]	D140-T30-E50	762	0.64	Axial + Ec.	30	1260	1103	1.14
67		D140-T400-E50	831	0.64	Axial + Ec.	395	1374	1331	1.03
68		D140-T600-E50	887.2	0.64	Axial + Ec.	620	1314	1383	0.95
69		D140-T900-E50	427	0.65	Axial + Ec.	883	696	752	0.93
70		D140-T1100-E50	342.6	0.64	Axial + Ec.	1095	595	625	0.95
71		D168-T30-E50	776.5	0.51	Axial + Ec.	30	746	694	1.08
72		D168-T400-E50	790.0	0.51	Axial + Ec.	395	770	690	1.12
73		D168-T600-E50	796.7	0.51	Axial + Ec.	620	744	666	1.12
74		D168-T900-E50	383.4	0.51	Axial + Ec.	883	429	406	1.06
75		D168-T1100-E51	252.1	0.51	Axial + Ec.	1095	281	257	1.09
76	Zhong et al. (2022 (a)) [22]	S1-T30	814.2	0.53	Axial	30	1272	1172	1.08
77		S1-T400	830.9	0.53	Axial	395	1311	1309	1.00
78		S1-T600	859	0.53	Axial	620	1371	1309	1.05
79		S1-T900	408.4	0.53	Axial	883	680	655	1.04
80		S1-T1100	282.8	0.53	Axial	1095	475	460	1.03
81		S1-T30	762	0.55	Axial	30	2698	2612	1.03
82		S1-T400	831	0.56	Axial	395	3088	3461	0.89
83		S1-T600	887.2	0.55	Axial	620	3189	3200	1.00
84		S1-T900	427	0.56	Axial	883	1530	1670	0.92
85		S1-T1100	342.6	0.56	Axial	1095	1250	1341	0.93

Table 3. Details of experimental specimens considered for validation (continued)

Sl.No.	Author-s	Specimen Name	Yield strength (f_{yt})	$\bar{\lambda}_{20}$	Load type	Temp. (°C)	Exp. Load (kN)	F.E.A Load (kN)	$P_{exp.}/P_{F.E.A.}$
86	Ye and Ozaki (2021) †[29]	λ – 40, T-30°C	397	0.56	Axial	20	217	190	1.14
87		λ – 40, T-200°C	448	0.56	Axial	200	245	253	0.97
88		λ – 40, T-300°C	408	0.56	Axial	300	246	238	1.04
89		λ – 40, T-400°C	401	0.56	Axial	400	230	236	0.97
90		λ – 40, T-500°C	390	0.56	Axial	500	204	232	0.88
91		λ – 40, T-600°C	345	0.56	Axial	600	207	206	1.01
92		λ – 40, T-700°C	314	0.56	Axial	700	147	191	0.77
93		λ – 40, T-800°C	270	0.56	Axial	800	145	174	0.84
94		λ – 50, T-30°C	397	0.7	Axial	20	212	167	1.27
95		λ – 50, T-200°C	448	0.7	Axial	200	207	229	0.90
96		λ – 50, T-300°C	408	0.7	Axial	300	209	233	0.90
97		λ – 50, T-400°C	401	0.7	Axial	400	220	214	1.02
98		λ – 50, T-500°C	390	0.7	Axial	500	178	210	0.85
99		λ – 50, T-600°C	345	0.7	Axial	600	190	191	0.99
100		λ – 50, T-700°C	314	0.7	Axial	700	135	179	0.75
101		λ – 50, T-800°C	270	0.7	Axial	800	125	165	0.76
† Square hollow sections					Mean ($P_{exp./}P_{F.E.A}$) = 1.096				
S. D = 1.113, C. O. V = 0.011									

Table 4. Proposed post-fire reduction for F_y - 310 CFS steel by [35]

Post-fire property	Post-fire retention factor	Temperature range
$\frac{E_t}{E_{20}}$	-0.00035 x t +1.0121	$23 \leq t < 308$
	0.85	$308 \leq t \leq 1000$
$\frac{\sigma_{y,t}}{\sigma_{y,20}}$	1	$23 \leq t \leq 308$
	-0.0009 x t +1.277	$308 < t \leq 1000$
$\frac{\sigma_{u,t}}{\sigma_{u,20}}$	1	$23 \leq t \leq 411.5$
	-0.0007 x t +1.29	$411.5 < t \leq 1000$

Table 5. Parameters selected for the parametric study

Sl. No	Name	Outer dia.	Thic-kness	Len-gth	Eff. length	Eccentricity (mm)					
						e0 = 0	e0 = 0.25Do	e0 = 0.75Do	e0 = 1.5Do	e0 = 2.5Do	e0 = 4Do
1	CBC-T1000-E11.1	74.82	6.46	541	695	0	19	56	112	187	299
2	CBC-T1000-E25.9	75.06	6.53	540	694	0	19	56	113	188	300
3	CBC-T1000-E46.3	75.29	6.52	541	695	0	19	56	113	188	301
4	D73-L6-T1000	72.85	2.77	438	548	0	18	55	109	182	291
5	D73-L9-T1000	72.65	2.77	658	768	0	18	54	109	182	291
6	D89-L6-T1000	88.98	2.76	534	644	0	22	67	133	222	356
7	D168-T1100-E50	167.5	3.88	1501	1641	0	35	104	209	348	557
8	D140-T1100-E50	139.2	9.92	1501	1641	0	42	126	251	419	670
9	Q235-60-60	60	3.5	1050	1200	0	15	45	90	150	240
10	Q235-60-80	60	3.5	1450	1600	0	15	45	90	150	240

11	Q235-60-100	60	3.5	1850	2000	0	15	45	90	150	240
12	Q235-89-60	89	4	1650	1800	0	22	67	134	223	356
13	Q345-60-60	60	3.5	1050	1200	0	15	45	90	150	240
14	Q345-60-80	60	3.5	1450	1600	0	15	45	90	150	240
15	Q345-60-100	60	3.5	1850	2000	0	15	45	90	150	240
16	Q345-89-60	89	4	1650	1800	0	22	67	134	223	356
17	S1-T1100	139.2	3.92	1200	1310	0	35	104	209	348	557
18	S2-T1100	139.3	9.88	1200	1310	0	35	105	209	348	557
19	SR40-600	50	3.2	750	720	0	13	38	75	125	200
20	SR50-600	50	3.2	950	920	0	13	38	75	125	200

Table 6. Accuracy of the proposed equation

Capacity estimation	Unheated columns		Fully heated columns		Parabolic heated columns (Real fires)	
EN 1993-1-1, Eq.8 [3]	Mean	1.732	Mean	1.65	Mean	2.183
	S. D.	0.333	S. D.	0.530	S. D.	0.7063
Revised EN 1993-1-1 Eq.13					Mean	1.425
					S. D.	0.452